Journal of ELECTRONIC MATERIALS, Vol. 44, No. 1, 2015
DOI: 10.1007/s11664-014-3429-2

Graphene-Based Hybrids with Manganese Oxide Polymorphs as Tailored Interfaces for Electrochemical Energy Storage: Synthesis, Processing, and Properties

S. GUPTA,[1,3,4] M.M. VAN MEVEREN,[1] and J. JASINSKI[2]

1.—Department of Physics and Astronomy, Western Kentucky University, 1906 College Heights Blvd., Bowling Green, KY 42101-3576, USA. 2.—Department of Chemical Engineering and Conn Center for Renewable Energy Research, University of Louisville, 1911 S. 3rd St., Louisville, KY 40292, USA. 3.—e-mail: sgup@rocketmail.com. 4.—e-mail: sanju.gupta@wku.edu

Technological progress is determined to a greater extent by developments of novel materials or new combinations of known materials with different dimensionality and diverse functionality. In this work, we report on the synthesis and characterization of graphene-based hybrid nanomaterials coupled with transition-metal oxide polymorphs (nano/micro-manganese oxides, i.e., β-MnO_2 [Mn(IV)] and Mn_3O_4 [Mn(II, III)]). This lays the groundwork for high-performance electrochemical electrodes for alternative energy devices owing to their higher specific capacitance, wide operational potential window and stability through charge–discharge cycling, environmentally benignity, cost-effectiveness, easy processing, and reproducibility on a larger scale. To accomplish this, we strategically designed these hybrids by direct anchoring or physical adsorption of β-MnO_2 and Mn_3O_4 on variants of graphene, namely graphene oxide and its reduced form, via mixing dispersions of the constituents under mild ultrasonication and drop-casting, resulting in four different combinations. This facile approach affords strong chemical/physical attachment and is expected to result in coupling between the pseudocapacitive transition-metal oxides and supercapacitive nanocarbons showing enhanced activity/reactivity and reasonable areal density of tailored interfaces. We used a range of complementary analytical characterization tools to determine the structure and physical properties, such as scanning electron microscopy combined with energy-dispersive x-ray spectroscopy, atomic force microscopy, x-ray diffraction, resonance Raman spectroscopy combined with elemental Raman mapping, and transmission electron microscopy in conjunction with selected-area electron diffraction. All of these techniques reveal surface morphology, local (lattice dynamical) and average structure, and local charge transfer due to the physically (or chemically) adsorbed manganese oxide of synthesized hybrids that helps to establish microscopic structure–property–function correlations highlighting the surface structure and interfaces to further investigate their electrochemical supercapacitor properties.

Key words: Graphene derivatives, manganese oxide polymorphs, charge transfer, surface structure and tailored interface, Raman mapping, HRTEM and SAED, energy storage

INTRODUCTION

Graphene is a single atomic layer of sp^2-bonded carbon (sp^2 C) in which the carbon atoms are bonded together in a hexagonal lattice resembling a

(Received August 14, 2014; accepted September 17, 2014; published online October 10, 2014)

honeycomb.[1,2] It has several unique superlative physical properties such as an ambipolar electric field effect, high mobility of charge carriers (~20,000 $cm^2\ V^{-1}\ s^{-1}$), anomalous quantum Hall effect,[3] and massless relativistic carriers. All of these properties make graphene appropriate for many potential applications including graphene nanoribbon transistors, single-molecule gas detectors, and transparent conducting electrodes. Moreover, field-effect transistors based on graphene are now considered a candidate for post-silicon and radiofrequency (RF) electronics. It also exhibits a high theoretical specific surface area ($2630\ m^2\ g^{-1}$)[4] and remarkable mechanical strength and flexibility (Young's modulus ~1 TPa)[5] suitable for super(ultra)capacitors[6,7] and Li-ion battery anodes.[8]

In addition, graphene can be modified through a variety of chemical interactions/moieties to form numerous graphene derivatives with tailored and desirable properties.[9] Graphene oxide (GO)[10,11] and reduced graphene oxide (rGO)[12] are graphene variants emerging as novel functional nanoscaffolds for use in physical, chemical, and biological applications, including semiconductor materials in transistors,[13] liquid-crystal devices,[14] hydrogen-based energy storage devices,[15] electrochemical biological sensors,[16] nanomedicine,[17] supercapacitors,[18,19] batteries,[20] solar cells,[21] and fuel cells.[22,23] In fact, GO recently emerged as a solution-processable material for large-area electronics because it can be readily and uniformly deposited on a range of substrates and reduced by various means. While GO can be considered as the insulating (due to the presence of saturated sp^3-bonded carbon atoms bound to oxygen) and disordered analog of the highly conducting crystalline graphene with oxygenated functional groups (carboxyls or –COOH and epoxides or –ROOH at the edges and hydroxyls or –OH on the surface), its reduced form (rGO) containing residual (~8 at.%) oxygen and possibly amine groups from hydrazine monohydrate permits semiconductor transition and offers tunable electrical conductivity over several orders of magnitude and *a priori* quasi-equivalent to graphene. The covalent oxygen functional groups give rise to remarkable mechanical strength[24,25] along with molecular-level chemical–biological sensing capability.[26–28] The C–O bonds possess differing chemical reactivity based upon their location and hybridization, owing to the electron-withdrawing effect of sp-hybridized oxygen (carbonyl groups) and the donating effects of sp^2-hybridized oxygen (alcohol groups). In addition, the presence of a few sp^3 C sites disrupts the flow of charge carriers through sp^2 clusters so that electrical transport in rGO occurs primarily by hopping rather than near ballistically,[29] as is the case for traditional, mechanically exfoliated graphene. Moreover, these chemical modifications can further tailor the surface chemistry to specific applications, including hydrophilic versus hydrophobic (GO) behavior, facilitating feasible interactions and surface and interface structure dependent electrocatalytic activity, especially when combined with other nanoscale materials.[28,30,31]

Also, due to the lack of detailed knowledge on the bonding configuration, location of the residual oxygen, density and type of defects generated during oxygen evolution, and the hybridization states of C–C and C=O bonds and their spatial distribution, understanding of the exact nature of the electronic structure is limited. However, this limited knowledge and information on rGO and GO does not prevent their development with other materials to form hybrids with facile surface structure and tailored interfaces for electrochemical applications as presented in this work. This is due to the wide proliferation of portable consumer electronics, where much effort has been devoted to lightweight, flexible, and even wearable electronics to meet growing demands from modern society, being applicable for wearable displays, artificial electronic skin, and distributed sensors.[32,33]

Electrochemical systems represent some of the most efficient and environmentally friendly energy technologies exhibiting growing demand. Owing to their unique power and energy density range, they fill the gap between traditional capacitors and batteries by enabling supercapacitors, which play a vital role in energy storage and conversion.[34,35] Typical supercapacitive electrode materials include carbon-based nanomaterials, conducting polymers, and transition-metal oxides.[36–43] While supercapacitors based on a gamut of nanocarbons including activated carbon, porous carbon, carbon nanotubes, and now graphene have been investigated, they by themselves are performance limited (in terms of power and energy density). As a result, novel functional materials with greater performance become indispensable and breakthroughs happen when new types of materials or new combinations of known materials with different dimensionality and functionality are created. To address these issues, pseudocapacitive (alternatively, redox-active) materials such as oxides, hydroxides, and polymers are being explored for supercapacitors with increased specific capacitance and high energy density. Metal oxides (MeO_x) represent an attractive type of material with high specific capacitance, wide operational potential window (required for Faradaic redox reactions), and stability through multiple cycling. Among several redox-active materials (e.g., RuO_2, TiO_2, Co_3O_4, V_2O_5, Fe_2O_3, CoO, NiO, MoO_2, etc.),[42–45] recent research has shown that manganese oxide polymorphs (i.e., MnO_2 and Mn_3O_4) appear to be the most promising materials. The latter offer advantages of relative cost-effectiveness, simplicity, scalable synthesis and processability, environmental benignity (being harmful only by excessive inhalation), and rich electrochemical properties [rapid charging–discharging with various oxidation states ($Mn^{2+}/Mn^{3+}/Mn^{4+}$)].[46] Mn_3O_4 is a unique mixed-valence oxide

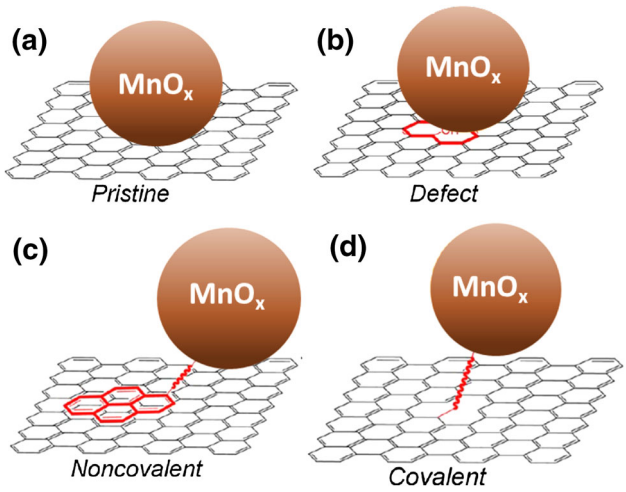

Fig. 1. (Color online). Schematic illustrations of four different types of transition-metal oxide nanoparticle (TMeONP)–graphitic interface: (a) pristine interface where TMeONP and pristine graphitic surfaces are in direct contact, (b) TMeONP–defect interface where atoms of TMeONP are bonded to defect sites of the graphitic surfaces, (c) noncovalent interface or physisorption where functional moieties of graphitic surfaces interact through noncovalent interactions with TMeONP, and (d) covalent interface where covalent bonding or chemisorption between graphitic surface and its functional moieties and TMeONPs is formed.

which adopts a tetragonally distorted spinel structure at ambient conditions.[47] The other polymorph β-MnO_2 crystallizes in the rutile crystal structure with three-coordinate oxide and octahedral metal centers.[48] β-MnO_2 is characteristically nonstoichiometric, being deficient in oxygen.

Graphene-based two-dimensional (2D) and three-dimensional (3D) hybrid materials open up new frontiers in science and technology and expand the scope of graphene applications as synergistic effects can result from the interaction between graphene and nanomaterials supported on/in the graphene.[49–52] Figure 1 illustrates a range of possible transition-metal oxide nanoparticle (TMeONP)–graphitic interfaces that can be formed either separately or concurrently. Hybrid systems combine materials of different natures, like composite materials, but unlike the latter, the constituents are usually bound by some interaction, be it strong, for example, covalent-like,[53] or weak, as in some layered materials intercalated with polymers.[54] The concept of the hybrid system extends to situations in which, despite the absence of a bond between the compounds, at least one of the compound's properties influences those of the other compounds, leading to combined or novel functions, which is the case herein.[55] This broad definition of a hybrid system encompasses systems whose properties are governed by proximity effects, for example, proximity-induced superconductivity. In sp^2-bonded graphite and other nanocarbon systems, interface atoms are an important, if not the main, constituent of the hybrid system. This is a general characteristic of hybrid materials based on sp^2 C resulting from the topography of these forms of carbon. This is an attractive feature, since in many cases the extent to which the hybrid system's properties can be engineered is related to the role of interfaces.[56] Most systems referred to as graphene-based hybrids are prepared following chemical routes. It is widely known that GO and rGO can serve as both a supporter and a conduction path for shuttling electrons involved in redox reactions during electrochemical processes.

In this study, this is clearly the case and will indiscriminately enhance the electrochemical activity of the different graphene-based hybrids. In spite of substantial research activity, keeping in view the insights into surface and/or local charge transfer and interfacial aspects, knowledge on the microscopic structure and property relationships is limited. *p*- and *n*-type doping of graphene achieved through surface transfer doping or substitutional doping and applications based on doping are of great importance. This is because it is beneficial to design high-performance electronic devices based on chemically doped graphene. Recently, metal adatoms and clusters on graphene have been a topic of great interest, and it is expected that they locally dope or modify the band structure.

We aimed to develop 3D hybrid nanomaterials by utilizing GO and rGO (supercapacitive) coupled with β-MnO_2 and Mn_3O_4 (pseudocapacitive)[57] for use in electrochemical applications. It is noteworthy that, in practical supercapacitor electrodes, two energy storage mechanisms often work rather concomitantly. There is a considerable impact of nanotechnology on the electrochemical properties of manganese oxide nanomaterials with desired and uniform structures for energy storage applications. We strongly believe that such interfaces can offer additional electrolyte-transport paths for electron transfer and proton/cation diffusion due to their 3D interconnected tunnel crystal phase and unique microspherical architecture constructed from small nanoparticles. The strategic choice of MnO_2 and Mn_3O_4 is due to their higher specific capacitance, wide operational potential window and stability through charge–discharge cycling, and environmentally benignity, creating novel functional hybrid nanomaterials that are cost-effective, easily processable, and reproducible on a larger scale; they are investigated in terms of structure and physical properties, highlighting the surface structure and interfaces.

EXPERIMENTAL PROCEDURES

Sample Preparation

To synthesize thin films of GO (Graphene Supermarket, TX), rGO (Graphenea Inc., Spain), and their hybrids with two polymorphs of manganese oxide (β-MnO_2, Mn_3O_4) (US-nano, TX) nanopowders, concentrations of 0.085 mg mL^{-1} GO (and rGO), 0.2 mg mL^{-1} β-MnO_2, and 0.09 mg mL^{-1}

Mn_3O_4 were used. GO was prepared in deionized (DI) water. rGO was prepared via a modified Hummer's method followed by chemical reduction using hydrazine monohydrate.[58–61] We made suspensions/dispersions of 10 mL each in Milli-pure (Milli-Q) water by stirring each of these solutions mildly for around 1 h at room temperature followed by ultrasonication for around 40 min of the constituents. Each dispersion of graphene-based material was individually combined/mixed with each manganese oxide in 1:1 ratio by volume to form hybrid solutions used in this study to determine an optimized configuration via mild ultrasonication for 30 min. Thin films of each of these samples were made by allowing a few drops of the solution to air-dry on commercial Si(001) substrates coated with 285 nm SiO_2, forming thin films of approximately 1 cm^2. This approach affords strong attachment and is expected to provide coupling between the pseudocapacitive transition-metal oxides and nanographenes, leading to enhanced activity/reactivity. A complete list of the materials in the reference samples S1 to S8 is presented in Table I.

Sample Characterization

Scanning electron microscopy (SEM) images were taken on a JEOL (model 5400LV, MA) instrument operating with a thermionic emission gun (tungsten filament) at different primary electron acceleration voltages (V_{acc}) in secondary-electron imaging (SEI) mode, providing a topographical image collected with an in-lens detector, also equipped with an ISIS x-ray energy-dispersive spectroscopy (EDS) system. While it can be operated in both backscattered-electron imaging (BEI) and SEI modes, we specifically used SEI for imaging and BEI for EDS elemental composition contrast, both at V_{acc} = 10 kV with constant current of 45 μA. Atomic force microscopy (AFM) was performed in contact and noncontact modes in ambient conditions using a PicoPlus instrument (series 5500; Molecular Imaging Inc., MI). The AFM tips were made of silicon with nominal resonant frequency and spring constant of 15 kHz and 0.4 N m^{-1}, respectively; we used a scan speed ranging from 1 μm s^{-1} to 10 μm s^{-1} depending on the image size, a lateral optical sensitivity level ≤1 μV, and the manufacturer's stated tip radius of curvature when first used of < 10 nm (ContAl; BudgetSensors, Bulgaria). Friction force was also obtained by dividing the friction signal difference between the forward and reverse scans by two. Samples for high-resolution transmission electron microscopy (HRTEM) and selected-area electron diffraction (SAED) were prepared by placing one to two drops of individual component and of hybrids on commercial lacey-carbon Cu grids (Ted Pella Inc., CA) and allowing to dry in air, giving several regions and a sufficient number of isolated flakes and particles. HRTEM measurements provided the nanoscale structure morphology and helped to determine the interplanar spacing semiquantitatively. TEM images and SAED patterns were taken using a FEI Tecnai™ (model G2 F20) instrument operating at 200 kV and 1 nA with a Titan Themis charge-coupled device (CCD) camera. For SAED, two apertures (0.23 μm and 1 μm) were used, with a small spot size and spread beam to increase the electron coherence length at the sample. Raman spectra of all samples were measured to determine the lattice vibration characteristics at various areas of interest on the nanostructure and hybrid coating surfaces. The Raman spectra were recorded using a micro-Raman spectrometer (model InVia; Renishaw plc., UK) equipped with an excitation laser with wavelength of 632.8 nm (or energy E_L = 1.92 eV) and maximum power of 18 mW (~4 mW to 6 mW incident at the sample), with edge filters cutting at ~100 cm^{-1}. The scattered light from the sample was collected in backscattered geometry, transmitted by a beam splitter, and detected by a CCD camera. A 50× objective lens was used, providing a spot size of 2 μm to 3 μm. Extreme care was taken to avoid sample damage or laser-induced thermal degradation. The reflected light was filtered using an edge filter to remove the laser excitation and sent to a spectrometer. The Raman shift ranged from 400 cm^{-1} to 3200 cm^{-1} for Mn-containing hybrids whereas for GO and rGO it was kept between

Table I. Summary of GO and rGO and their hybrids with nano/micro-manganese oxides, i.e., β-MnO_2 [Mn(IV)] and Mn_3O_4 [Mn(II, III)], prepared using mild ultrasonication followed by drop-casting and drying at room temperature (RT)

Sample ID	Sample Material Specification
S1	GO (oxidized form of graphene with functional groups attached at edge and basal plane)
S2	rGO (reduced form of graphene oxide, equivalent of graphene)
S3	β-MnO_2 [manganese(IV) oxide; pyrolusite]
S4	Mn_3O_4 [manganese(II, III) oxide; hausmannite]
S5	S1 + S3 (drop-cast on SiO_2/Si wafers and air-dried at RT)
S6	S1 + S4 (drop-cast on SiO_2/Si wafers and air-dried at RT)
S7	S2 + S3 (drop-cast on SiO_2/Si wafers and air-dried at RT)
S8	S2 + S4 (drop-cast on SiO_2/Si wafers and air-dried at RT)

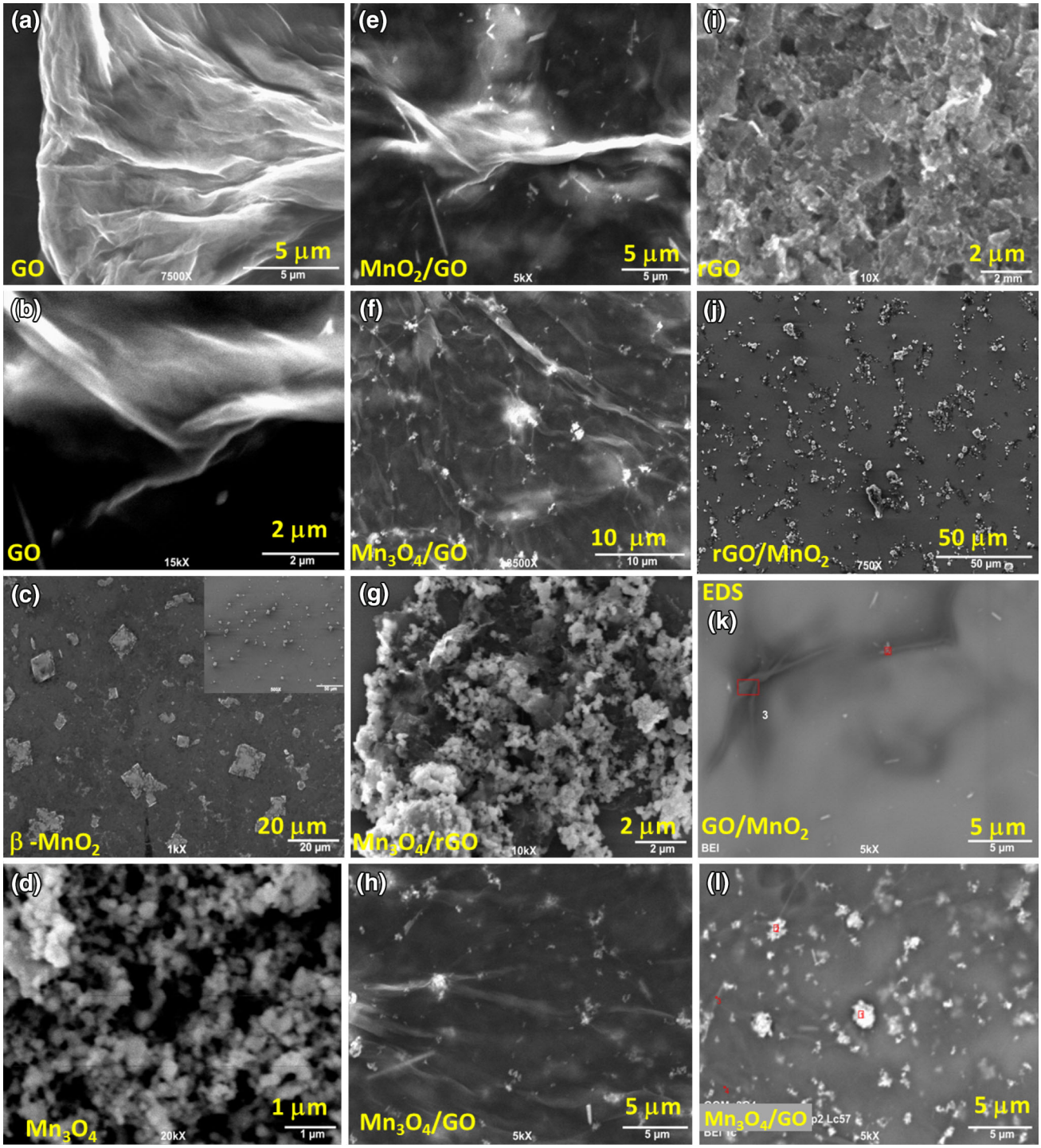

Fig. 2. (Color online). SEM images of GO and rGO and their hybrids with nano/micro-manganese oxides, i.e., β-MnO_2 [Mn(IV)] and Mn_3O_4 [Mn(II, III)], with V_{acc} of 10 kV in secondary-electron imaging (SEI) mode at constant current of ~45 μA. The corresponding BEI for GO/MnO_2 and GO/Mn_3O_4 are shown for EDS studies, helping to corroborate the presence of elements such as C and Mn and to determine the elemental composition at different spots on the sample (scale bars shown at bottom of images).

1150 cm^{-1} and 3200 cm^{-1} with spectral resolution of 1 cm^{-1}. The acquisition time per pixel was a few minutes to slightly less than an hour in the case of Raman mapping with spatial resolution of 0.2 μm (or 0.12 μm) (or 200 nm or 120 nm) for an area of 20 μm × 20 μm. To obtain more detail and greater understanding of the interaction between nanotubes and polymer, we also measured the average and local crystal structure. X-ray diffraction (XRD) was carried out using a Siemens (now Thermo

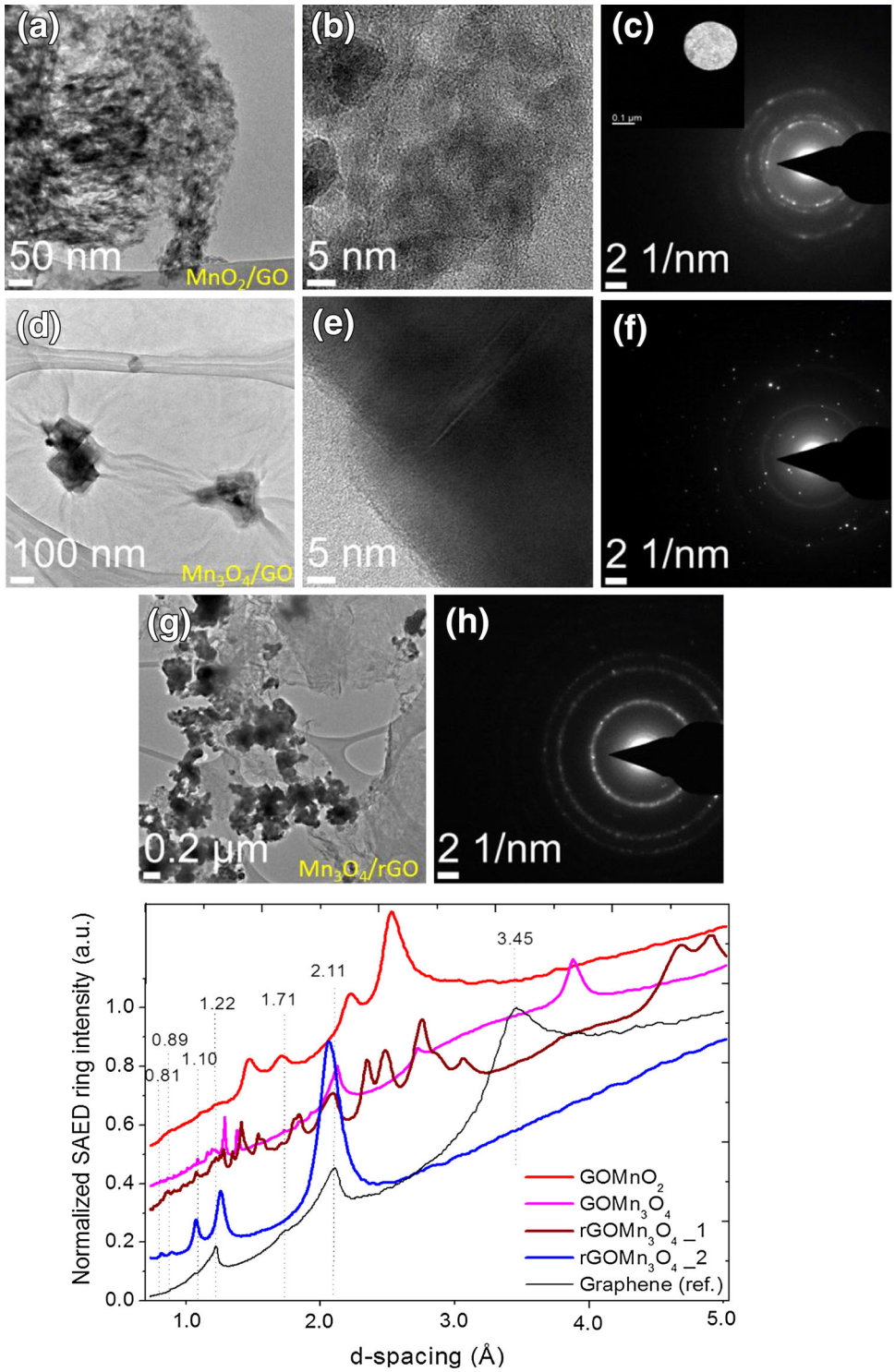

Fig. 3. (Color online). High-resolution transmission electron microscopy (HRTEM) images taken at 200 kV along with selected-area electron diffraction (SAED) results for aperture size of 200 nm of representative samples of (a) GO/MnO_2, (b) GO/Mn_3O_4, and (c) rGO/Mn_3O_4. The surface morphology exhibiting surface modulations and corrugated structures with small and large wrinkles is consistent with all kinds of microscopy techniques, albeit at different spatial length scales. For SAED, a condensate aperture of 0.20 μm in Köhler condition was used with a small spot size and spread beam to increase the electron coherence length at the sample. This allowed us to obtain a small, practically parallel beam with illumination angle of 0.16 mrad and area of 200 nm in diameter only. The diffraction peaks were recorded using a CCD for further quantitative analysis. The GO/rGO rings and diffraction spots of MnO_2 and Mn_3O_4 are apparent. The corresponding real space (d_{hkil}) intensity pattern revealing the crystal structure of the hybrids is also provided. To find the intensity values, each of the Bragg reflections was fit using a Gaussian distribution, yielding peak intensities, positions, and widths (scale bars shown at bottom of images).

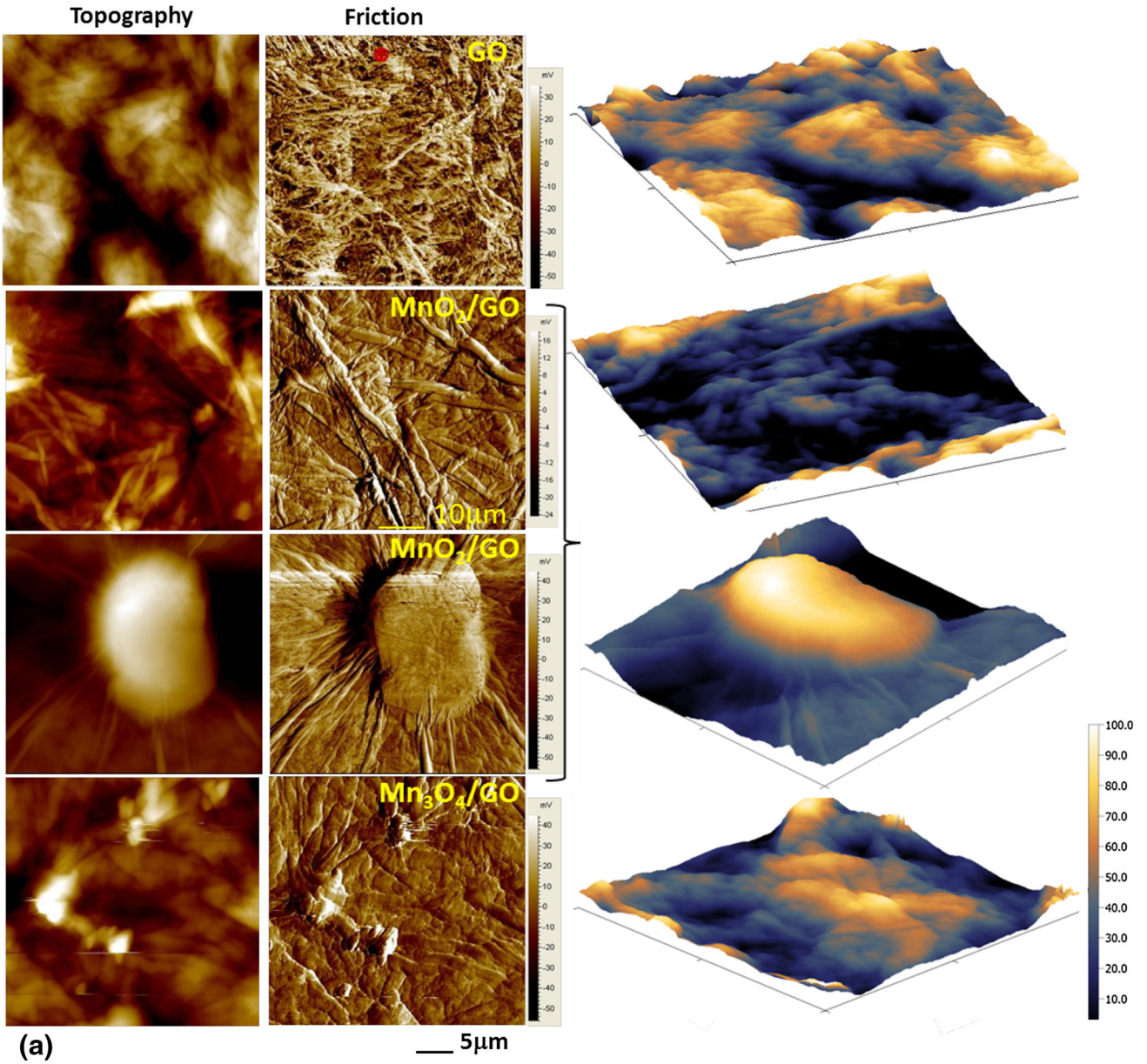

Fig. 4. (Color online). Atomic force microscopy (AFM) over 5 μm $\times$ 5 μm in contact mode showing (left panels) surface topography and (right panels) friction images along with a three-dimensional representation of the surface topography obtained using Gwyddion software for representative (a) GO and (b) rGO and their hybrids with nano/micro-manganese oxides, i.e., β-MnO_2 [Mn(IV)] and Mn_3O_4 [Mn(II, III)].

Scientific, MA) model D2000 instrument, with x-ray diffractograms acquired in Bragg–Brentano geometry ranging from 2θ of 8° to 70° using Cu K_α (λ = 1.5405 Å) as an x-ray source operating at voltage of 45 kV and current of 40 mA. Samples were analyzed at a scan rate of 0.04°/s, or for improved signal-to-noise ratio at a scan rate of 0.02°/s. For measurement of room-temperature electrical properties, we made electrical contacts using colloidal silver paste and attached a Cu wire for connection to a Keithley 2400 source meter (Keithley, OH). We measured the two-point contact resistance and determined the room-temperature electrical conductivity (σ_{dc}) of all of the samples studied.

RESULTS AND DISCUSSION

Effective characterization of metal oxide–graphitic interfaces is rather challenging compared with the straightforward overall hybrid morphology. The interactions at metal oxide–graphitic interfaces play essential roles in the synthesis (morphology control), properties (material performance), and applications of such nanohybrids.

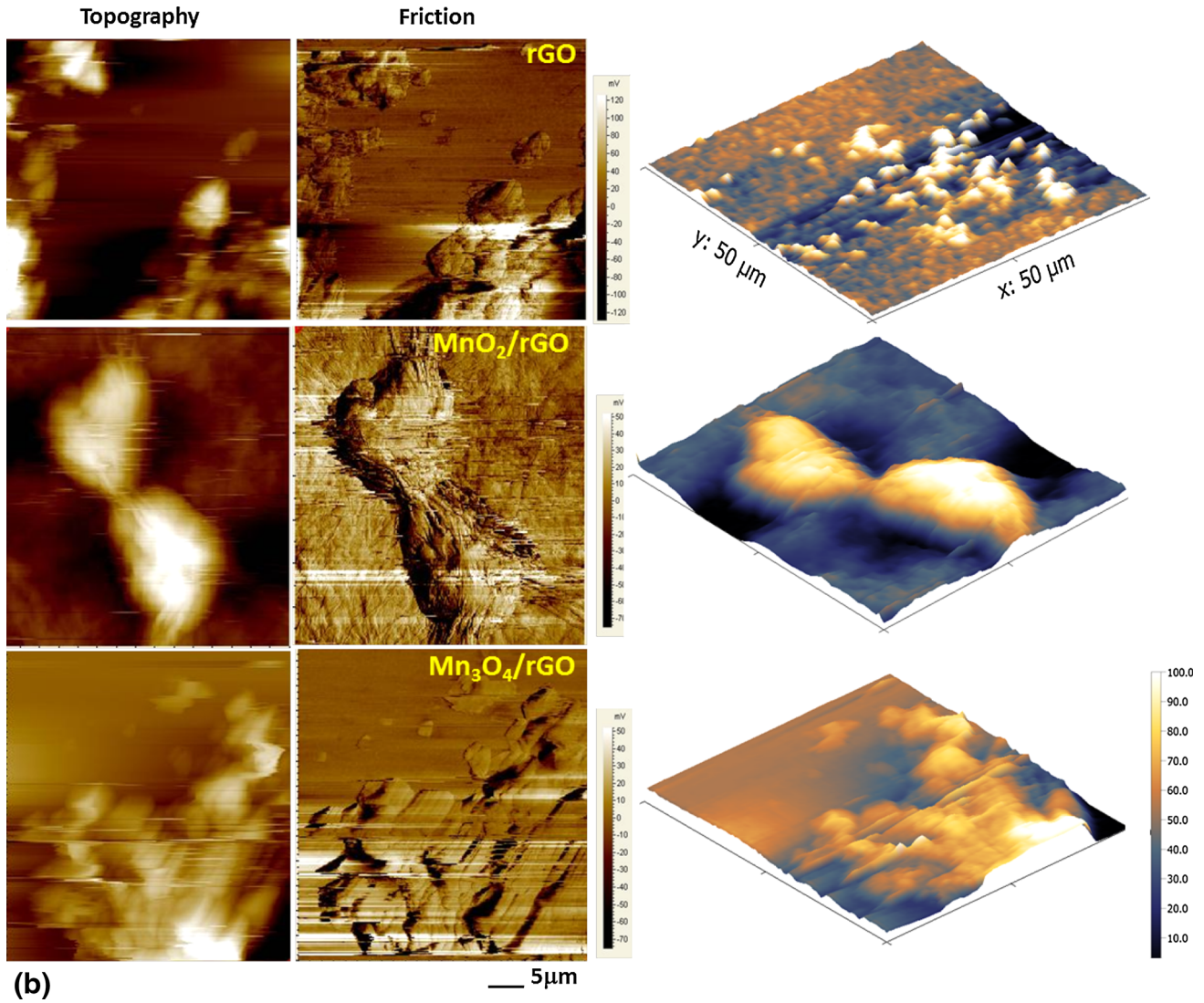

Fig. 4. continued.

Control and understanding of the interface will greatly promote the development of advanced metal–graphitic nanohybrid materials.[62] Figure 2 shows SEM micrographs obtained in SEI mode at various length scales of samples of constituents (GO, rGO, MnO_2, and Mn_3O_4) and of hybrids, revealing distinct surface morphology evolution, particle size and type variation (radiated spherulite versus spherical), number of GO nanowalls through thickness contrast and crumpled/wrinkled sheets, rGO flake size distribution, and homogeneity/uniformity of thin films with dense packing. Numerous aggregated nanoparticles with different shapes are observed, and their diameter varies between 20 nm and 80 nm. We also show BEI images and EDS analysis of representative samples of MnO_2/GO and Mn_3O_4/GO, revealing the elemental composition distribution (grey being low-Z C and O and dark being high-Z Mn), analysis of which confirms that the crystals are made of C, Mn, and O with chemical formula Mn_3O_4, including 85% Mn_3O_4 and 15% MnO_2, which is in agreement with a partially mixed system as verified by the XRD pattern below. Moreover, the red rectangles marked were used to determine the Mn/C ratio, which turned out to be 0.88 at.% and 0.30 at.%, respectively. This implies that, for each carbon atom, there is 0.0088 Mn and 0.003 Mn in these MnO_2/GO and Mn_3O_4/GO hybrids, respectively. The corresponding morphology was determined using TEM as shown in Fig. 3 at different magnifications along with SAED ring and intensity patterns. The graphene ring intensity pattern is included as a reference, and most of the peaks of the hybrids show graphene and GO peaks at 0.89 Å, 1.22 Å, 1.71 Å, and 2.11 Å. In the TEM images, crystalline defects such as stacking faults and dislocations are not found, and from the surface morphology at the nanoscale it is apparent that the

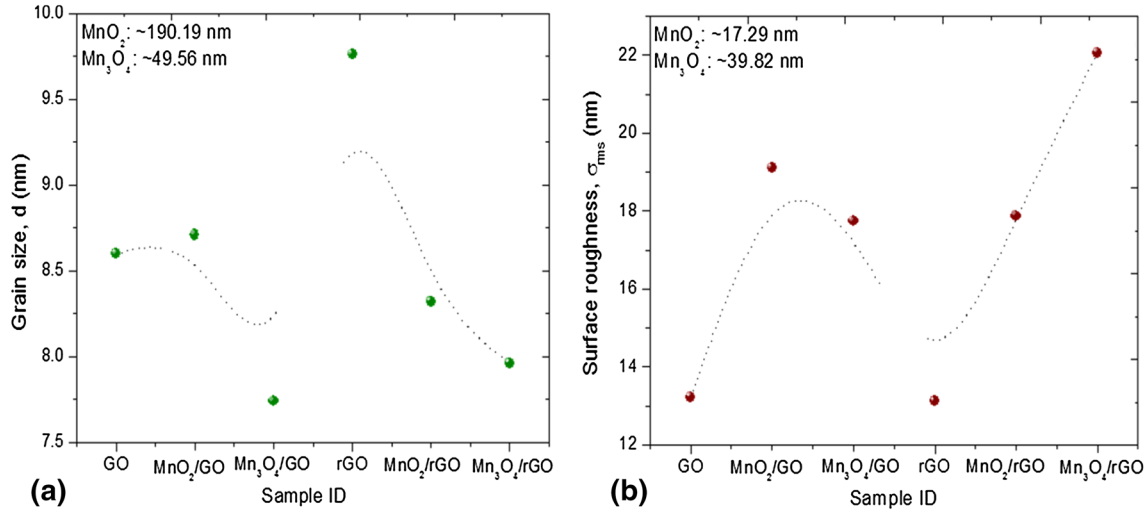

Fig. 5. (Color online). Variation of (a) grain size (d, nm) and (b) surface roughness (σ_{rms}, nm) deduced from AFM in Fig. 2 for all samples along with individual components.

metal-oxide nanoparticles are laid upon nanowalls/sheets of GO and rGO. The SAED pattern reveals an almost single-crystalline nature of the Mn oxides for which tetragonal and spinel structure can be indexed, in agreement with the XRD results discussed below. Figure 3 also shows that the general morphology of the as-prepared MnO_x nanoparticles consists of intertwined aggregates. Occasionally Mn_3O_4 presents a nanoctahedron shape consisting of two inverted pyramids attached at their square base and bounded by eight triangular facets, unlike MnO_2, which is rather either spherically shaped or nanorod- or needle-like. Moreover, these images show well-dispersed nanoparticulates anchored on graphene sheets/flakes/nanowalls. An enlarged TEM image shows lattice fringes with interplanar spacing d of 0.345 nm, corresponding to the (112) planes of Mn_3O_4 crystals, and 0.273 nm, which is equal to the lattice constant of the {200} plane of Mn_3O_4. On the other hand, the well-resolved SAED lattice fringes/rings give an interplanar spacing of 0.25 nm, in good agreement with the separation of the (211) and (103) planes for MnO_2.

Atomic force microscopy (AFM) images in two and three dimensions for 5 μm × 5 μm areas, showing the surface topography along with friction microscopy images, are provided in Fig. 4a and b for rGO/(MnO_2 and Mn_3O_4), and GO/(MnO_2 and Mn_3O_4), respectively. The corresponding analyses in terms of grain size (d) and root-mean-square surface roughness (σ_{rms}) are summarized in Fig. 5. It is apparent that there is an increase in σ_{rms} and a marginal change in d with the presence of manganese oxides on rGO and GO sheets. The AFM results provide an estimate of the size of the manganese oxide nanoparticles by themselves, with averages of 190 nm and 50 nm for MnO_2 and Mn_3O_4, respectively. The thickness difference determined through a line scan using Gwyddion software between each layer was ~0.42 nm, being marginally higher than anticipated (0.34 nm).[63]

X-ray diffraction (XRD) analysis was used to determine the crystallinity and phase of various forms by determining the lattice spacing and crystallite size. Figure 6a and b show XRD diffractograms of the constituents and of the hybrids displayed in Fig. 6c and d. The XRD pattern of GO is dominated by a single broad peak at 16.6°, which corresponds to an interlayer distance of 0.74 nm (Fig. 6a). This shows larger interplanar spacing than that of graphite, which is attributed to the expansion of galleries relative to the parent graphite (0.34 nm), consistent with oxidation of the graphene sheets and intercalation of water held in the interlayer galleries of hydrophilic GO. On the other hand, the pattern of the hydrazine-reduced rGO contains very broad reflections at 24.5° (corresponding to an interplanar spacing d of 0.36 nm), indicating restacking to form a poorly ordered graphite-like material, and a peak at ~12° which corresponds to a c-axis spacing of 0.69 nm. This is in addition to the peak at 16.6° similar to GO ascribed to residual carboxyls and hydroxyls groups in rGO, presumably induced by a bimodal or multimodal character of the interplanar spacing of rGO. Although the reduction mechanism of rGO is not known with certainty, it appears that the reduction starts from the edges of GO particles and proceeds into the basal planes. During the reduction, parts of the basal planes near the edges become reduced and subsequently snap together due to π–π^* interactions, thus narrowing the interlayer distance. Consequently, the reducing agent (hydrazine) cannot penetrate further into the interior of the rGO particles, presumably leading to the lower degree of reduction of rGO, corresponding to a c-axis spacing of 6.91 Å. All of the XRD peaks [MnO_2 and Mn_3O_4 (Fig. 6b)] can be indexed to tetragonal-phase and spinel-type hausmannite Mn_3O_4 [space group $I41amd$(141), Joint Committee on Powder Diffraction Standards (JCPDS) no. 44-0992] and pyrolusite MnO_2 (JCPDS no. 24-0735 and JCPDS no. 18-0803) phase including (110), (101), (112), (200), (211), (220), (310),

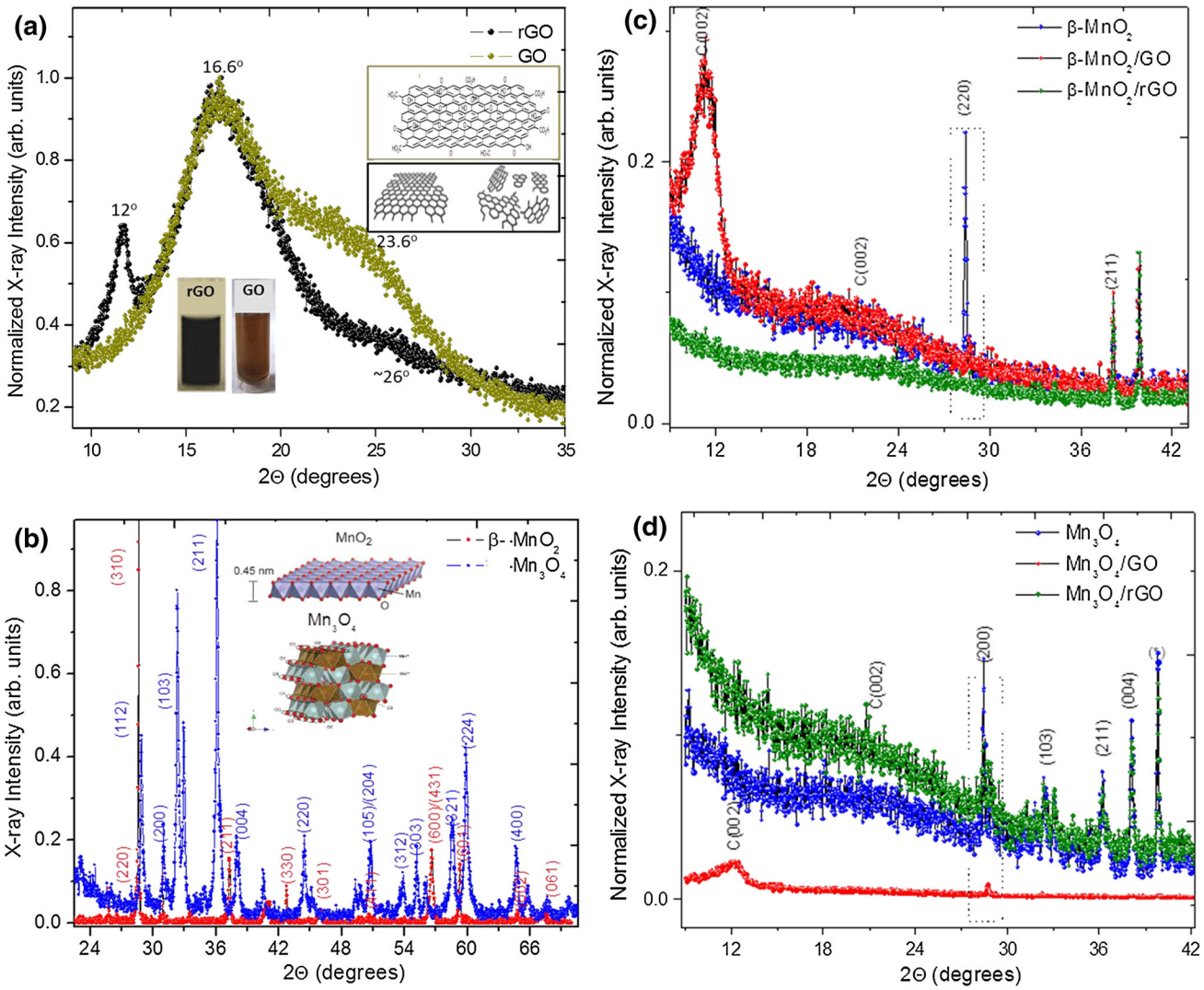

Fig. 6. (Color online). XRD diffractograms for the full region for (a) GO and rGO, (b) nano/micro-manganese oxides, i.e., β-MnO_2 [Mn(IV)] and Mn_3O_4 [Mn(II, III)], and (c, d) their hybrids, showing characteristic peaks in various regions. The peaks of interest for the hybrids are marked with either a dashed rectangular box or their (*hkl*) index. All of the diffractograms were taken in θ–2θ geometry with a Cu K_α x-ray source, i.e., with λ = 1.5405 Å.

(211), (301), (400), (411), and (600). The inset in Fig. 6b shows a schematic of the unit cell structure. No characteristic peaks from other impurities were detected. The Rietveld refinement procedure was performed to investigate the crystalline structure of the as-prepared nanocrystallite films of MnO_2 and Mn_3O_4. It can be shown that some of the main peaks at 2θ = 28.8°, 36.14°, and 65.09° can be correspondingly indexed to (002), (311), and (440) reflections of pyrolusite MnO_2 and of spinel-type Mn_3O_4.The peaks are sharper, indicative of better crystallinity with lattice constant of $a = b$ = 5.73 Å and c = 9.44 Å and $a = b$ = 4.41 Å and c = 2.87 Å based on (110), (101), and (211) planes.[64] The crystallite size was obtained from the XRD analysis using the Debye–Scherrer equation following the relation, $L_{hkl} = K\lambda/\beta_{hkl}\cos\theta_{hkl}$, where L_{hkl} is the crystallite size in nm, λ is the wavelength of Cu K_α, β_{hkl} is the full-width at half-maximum, and K = 0.94 is the shape constant. It can be seen that there is a marginal change in crystal size. The diffraction peaks of the hybrids are broad and of low intensity, while preserving the phases of the constituents (Fig. 5c and d), which implies the formation of true composites. The peak at 2θ = 28.8° was used to determine the lattice spacing (d_{hkl}) and particle size (L_{002}) of the hybrids, as shown by the analyses in Fig. 7a and b, respectively. A marginal increase in lattice spacing and particle size of the hybrid composites was apparent as compared with rGO and GO alone.

Raman Spectra of Free MnO_2 and Mn_3O_4

Raman spectroscopy (RS) is a technique sensitive to crystallization, local structural disorder, and defects in materials, being used to obtain information about the structure of the precursor phases and the graphene sheets in the hybrid composites

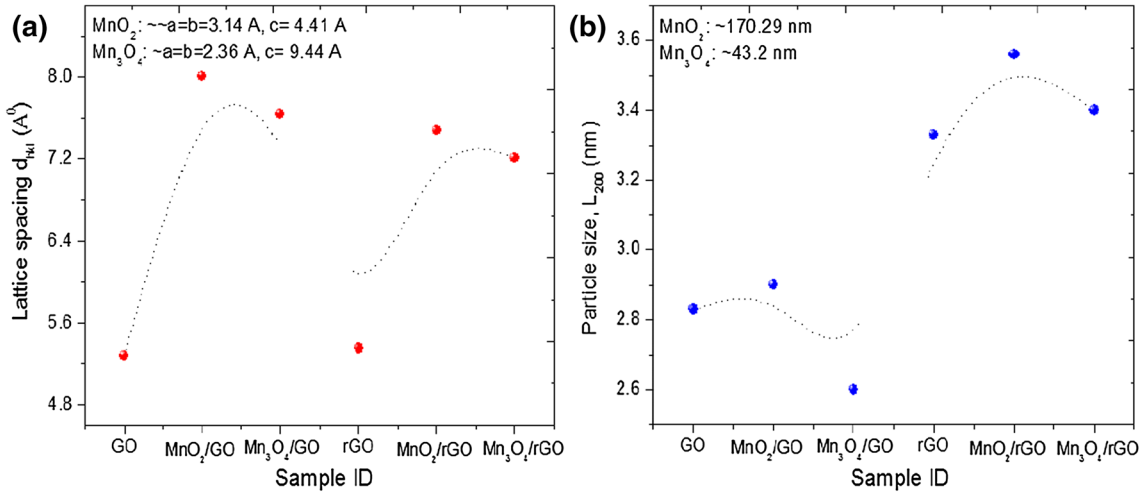

Fig. 7. (Color online). Variation of (a) lattice spacing (d_{hkl}, Å) from Bragg's law and (b) particle size (L_{200}, nm) determined using the Debye–Scherrer formula from the XRD results in Fig. 4 for all of the samples along with the individual components. The corresponding lattice constants (*a*, *b*, and *c*) for bulk β-MnO_2 [Mn(IV)] and Mn_3O_4 [Mn(II, III)] are also shown in (a).

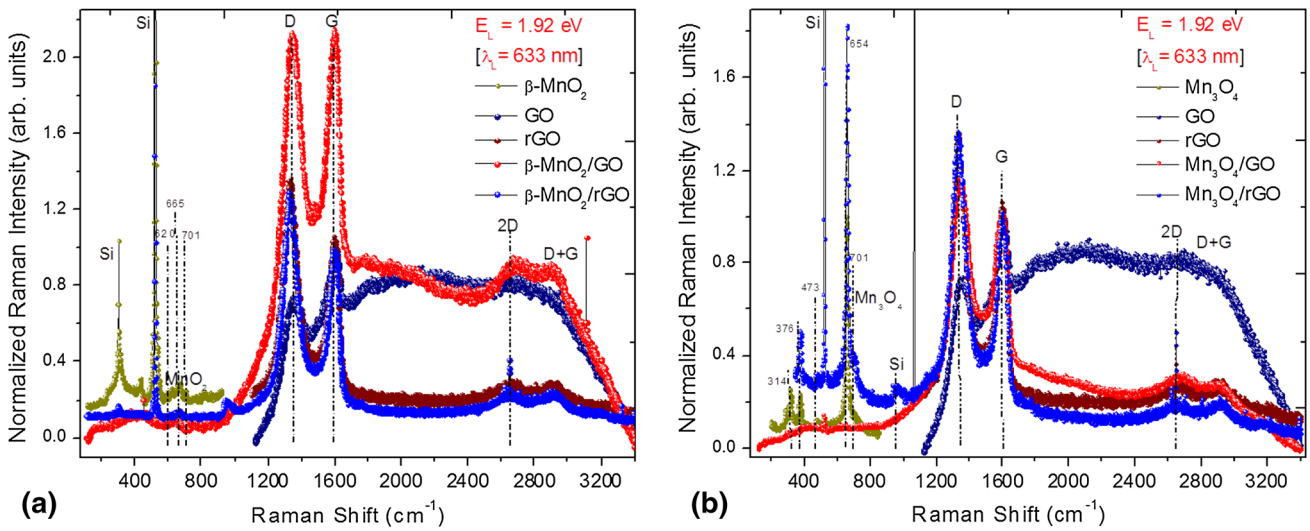

Fig. 8. (Color online). Representative micro-Raman spectra excited at wavelength of 633 nm (E_L = 1.92 eV), showing characteristic peaks for GO and rGO hybrids with nano/micro-manganese oxides, namely (a) β-MnO_2 [Mn(IV)] and (b) Mn_3O_4 [Mn(II, III)], in the 300 cm^{-1} to 3200 cm^{-1} spectral window.

(Fig. 8a and b). RS is well documented for various manganese oxides[65–68] and graphene-based systems,[69] but not for supported hybrids of manganese oxides. In this work, we attempted to investigate the possibilities to characterize these promising graphene-supported manganese oxide nanomaterials as electrochemical electrodes in terms of the local distribution of oxidic species on the graphene support and its evolution with increasing amount and different polymorphs of manganese oxide. Under the Raman microscope, the laser beam was focused on the surface of nanoparticulates and/or thin nanoneedle-like crystallites, and it was noted that there was minimal dependence of the spectra of the free manganese oxide polymorphs on the excitation laser wavelength applied (633 nm or 532 nm). The micro-Raman spectra of free Mn_3O_4 and MnO_2 nanoparticles consisted of four characteristic peaks at ~358.2 cm^{-1}, 480 cm^{-1}, 620 cm^{-1}, and 658 cm^{-1}, corresponding to skeletal vibrations, along with two weak bands at 450 cm^{-1} and 570 cm^{-1}, in good positional agreement with bulk tetragonal MnO_2 and Mn_3O_4 phases from the literature.[65,70]

MnO_2 was not found to be Raman-active by Strohmeier and Hercules[71] or Kapteijn et al.,[72] whereas Gosztola and Weaver[73] and Bernard et al.[74] reported well-defined spectra of this transition-metal oxide. In our spectra, MnO_2 has three major features that can be recognized at 500 cm^{-1}

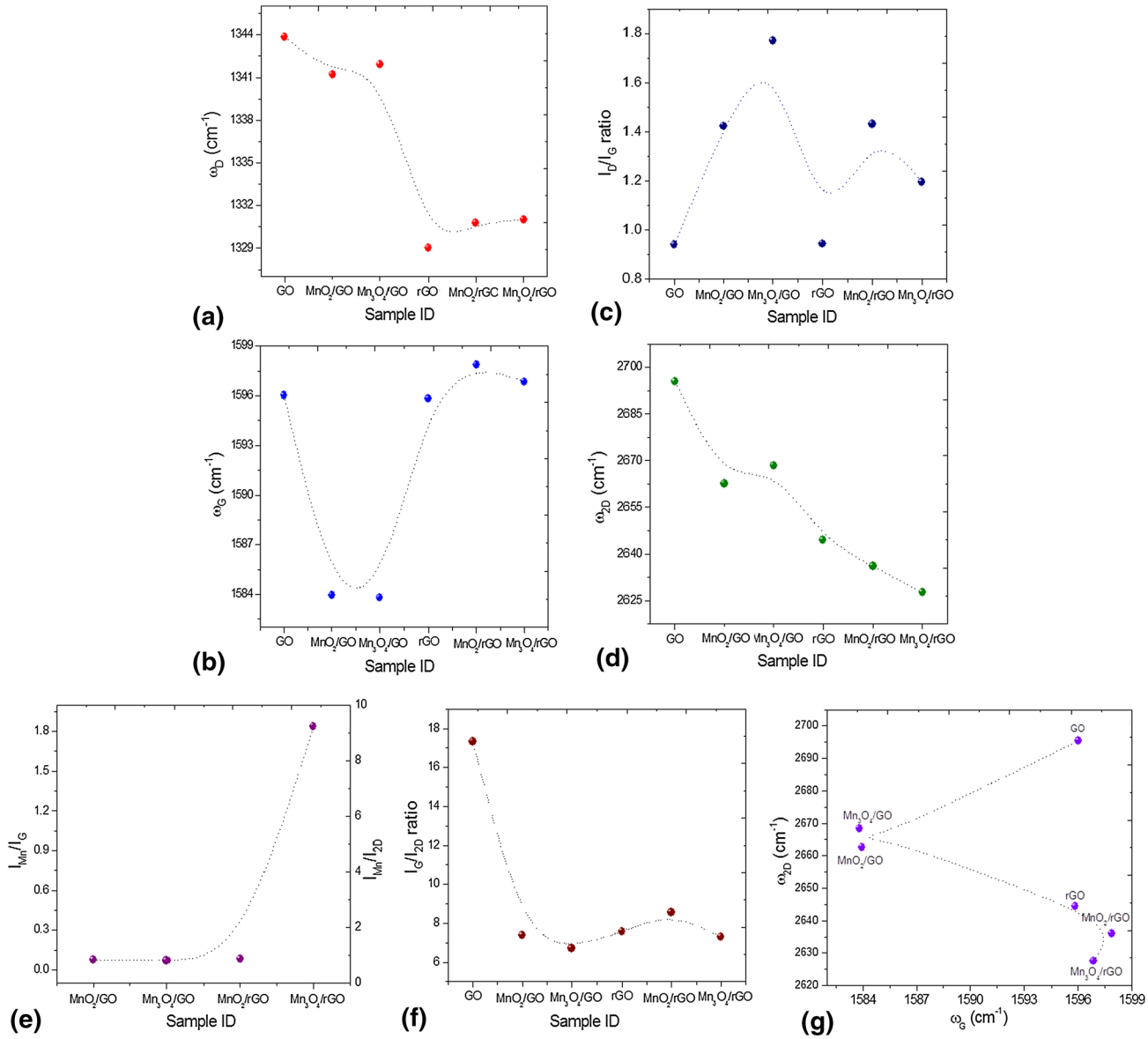

Fig. 9. (Color online). Variation of prominent Raman spectral bands for GO and rGO hybrids with nano/micro-manganese oxides, namely β-MnO_2 [Mn(IV)] and Mn_3O_4 [Mn(II, III)], in terms of (a) D band position (ω_D), (b) G band position (ω_G), (c) intensity ratio of D to G band (I_D/I_G), (d) 2D band position (ω_{2D}), (e) intensity ratio of Mn to G band (I_{Mn}/I_G), (f) intensity ratio of G to 2D band (I_G/I_{2D}), and (g) ω_{2D} versus ω_G band determining the defect type, i.e., residual or neutral versus charged (*p*- or *n*-type).

to 510 cm^{-1}, 575 cm^{-1} to 580 cm^{-1}, and 630 cm^{-1} to 640 cm^{-1}. The band at ~580 cm^{-1} was also observed in Ref. 72, being attributed to Mn–O lattice vibrations in MnO_2 or corresponding to distortion vibration of Mn–O in an octahedral environment in Mn_3O_4. Among the signals of the MnO_2 Raman spectrum in Ref. 73, the strongest bands lay at 523 cm^{-1}, 576 cm^{-1}, 633 cm^{-1}, and 650 cm^{-1}, the latter being assigned to Mn formed during the spectrum acquisition because of local heating of the sample. The intensity recorded for the band at 630 cm^{-1} to 640 cm^{-1} was, however, small compared with the same band in the Mn_3O_4 film. The appearance of a 633 cm^{-1} band in the case of MnO_2 excited with a 20-mW laser power was explained in Ref. 16 based on the formation of a new XM compound identified as γ-Mn_2O_3 with distorted hausmannite structure, an intermediate formed during decomposition of MnO_2 to Mn_3O_4. Therefore, the peaks at ca. 510 cm^{-1} and 580 cm^{-1} can be considered to be characteristic features of MnO_2. Mn_3O_4 gave a peak at 640 cm^{-1} to 650 cm^{-1} and a pair of features at ca. 314 cm^{-1}, 360 cm^{-1} to 390 cm^{-1}, and at ~480 cm^{-1}. Knowing that, regarding the oxidation state of the manganese ions, Mn_2O_3 is nearer to Mn_3O_4 than MnO_2, one can understand why Mn_2O_3 decomposed and the features of Mn_3O_4 are more pronounced in its Raman spectrum. What we consider to be a characteristic peak for Mn_2O_3 is the peak at 654 cm^{-1}, which also

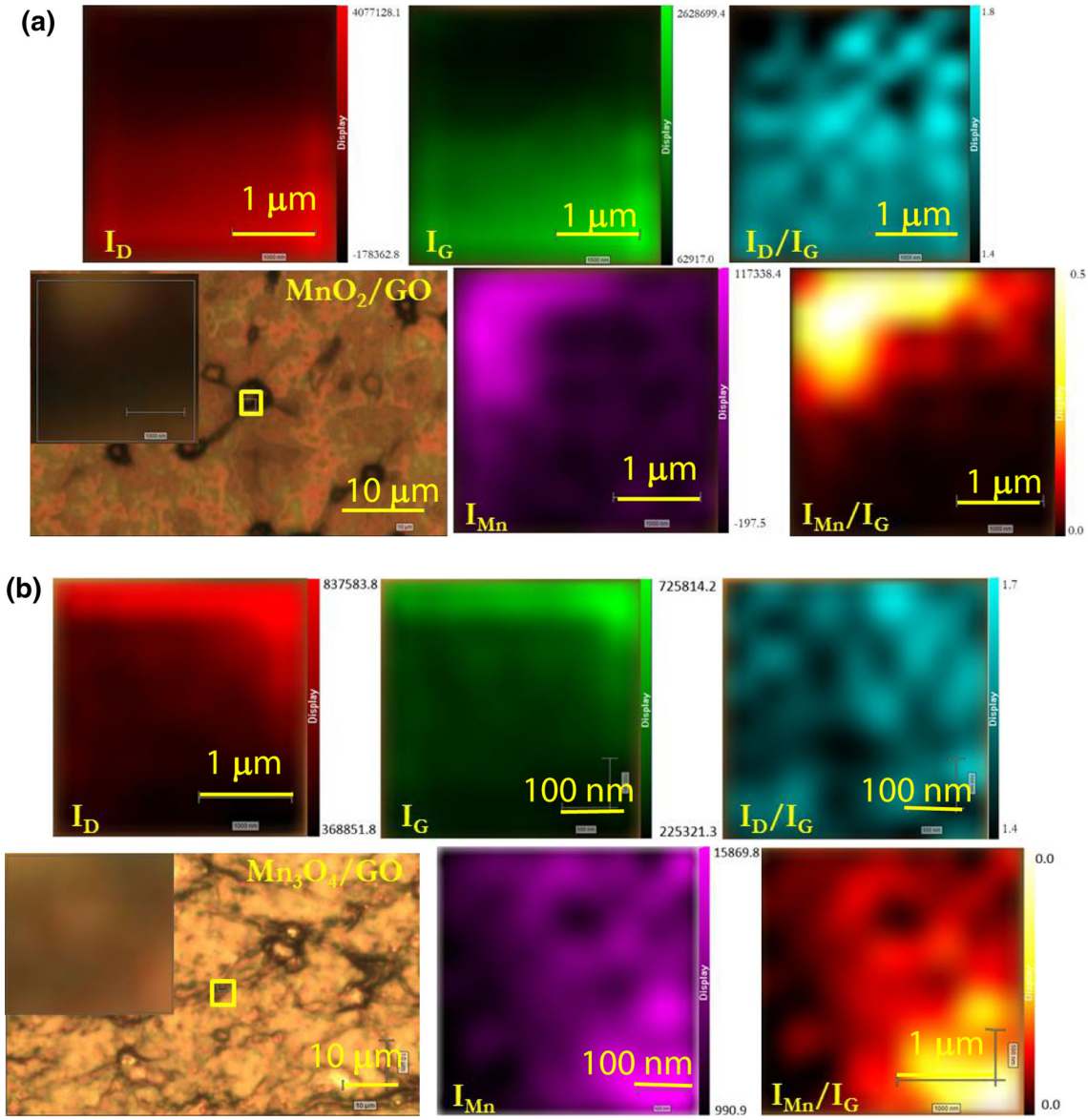

Fig. 10. (Color online). Raman mapping of representative hybrid samples of (a) MnO_2/GO and (b) Mn_3O_4/GO, in terms of intensity distribution of D, G, and Mn bands and their ratio to the G band. Corresponding optical micrographs taken with white or broadband light are also shown. The sharp and almost uniform maps of the D, G, and 2D bands contoured at the boundary are indicative of a higher degree of crystallinity/order. The elemental distribution of carbon and manganese and possible surface charge transfer are apparent. The black regions represent either the substrate (SiO_2) or the lower bound of the corresponding maps, as shown by the scale bar adjacent to each map.

appeared in earlier work[75] as the main feature of this oxide. In Ref. 71 the Mn_2O_3 spectrum, taken macroscopically, showed three weak peaks at 313 cm^{-1}, 653 cm^{-1}, and 697 cm^{-1}. Curiously there is no similarity between our Mn spectrum and that of Ref. 70, except for some differences between the relative peak heights and that Mn has the same feature as MnO_2. Due to symmetry considerations, the scattering for all Raman modes was rather strong, particularly for the 650 cm^{-1} mode, which can be assigned to the E_{1g} mode and attributed to a stretching mode of the Mn–O bond in MnO_6 octahedra, because the structural framework of the manganese oxides consists of MnO_6 octahedral units sharing corners and/or edges.[76–78] It is worth mentioning that, in MnO_2, Raman scattering results from a collective vibrational mode of the MnO_6 octahedron. The peaks at lower wavenumber correspond to the deformation modes of the metal–oxygen chain of Mn–O–Mn in the MnO_2 octahedral lattice. As the manganese atom is about five times heavier than the oxygen atoms, the vibrations of the Mn–O groups are supposed to involve mainly the oxygen atoms. The peak at 358 cm^{-1} is broad due to the smaller crystallite size, whereas the peak at 654 cm^{-1} is slightly asymmetric. This asymmetry may be attributed to the possible secondary crystalline phase MnO_2 and/or Mn_2O_3. The vibration

band located at 410 cm^{-1} is attributed to vibration of manganese species (Mn^{3+}–O) at the octahedral site of Mn_3O_4. The lower relative intensity for each vibrational mode may also be due to confinement of phonons by some crystal defects caused by Mn^{4+} vacancies, resulting in phonon decay and destruction of conservation of phonon momentum. The Raman peak intensity at 450 cm^{-1} and 405 cm^{-1} tends to disappear with smaller diameter, because as the nanoparticle size decreases, the number of surface atoms increases rapidly, having a large number of dangling bonds, and the coordination is incomplete, which can lead to crystal defects and partial breakdown of the Raman selection rules.

Raman Spectra of Graphene-Supported MnO_2 and Mn_3O_4

The optical appearance of the hybrids was highly inhomogeneous, with a rough yellowish dust or blackish surface spotted with dark-green islands. Raman spectra were taken on different points of the surface for relatively low loading of manganese oxides as presented in Fig. 8. A difference in the surface composition on going from one point to another is apparent, albeit marginal. The MnO_x layer was thin enough that the GO and rGO supports could be recognized and measured. The first- and second-order Raman spectra of the rGO and GO systems show two characteristic intense peaks, namely the G band at ~1580 cm^{-1} and 2D band at ~2670 cm^{-1}, which are assigned to the in-plane vibrational mode (E_{2g} phonon of the C_{sp2} atoms at the Brillouin zone center) and the intervalley double-resonance scattering of two TO phonons around the K-point of the Brillouin zone, respectively.[69] Another important peak at 1340 cm^{-1} is a defect-induced peak assigned to the D band activated by defects via an intervalley double-resonance Raman process, the D band activated by defects via an intravalley double-resonance process, and the combination mode of D and G modes (D + G band) at 2920 cm^{-1}, respectively.[69,79] Commonly, the frequency-integrated intensity ratio of the D to G band (I_D/I_G) can serve as a convenient measure of the amount of defects in graphitic materials, and the size of the sp^2 domains increases during reduction of GO.[69] The spectra were normalized with respect to the G band intensity. All of the Raman spectra were analyzed in terms of the D, G, and 2D band positions (ω_D, ω_G, and ω_{2D}), the intensity ratios of D to G (I_D/I_G), G to 2D (I_G/I_{2D}), and Mn to G (I_{Mn}/I_G), as well as the 2D versus G band position (ω_{2D} versus ω_G), the latter to determine the nature or type of defects (Fig. 9). While for GO-based hybrids, the D band varies between 1344 cm^{-1} and 1340 cm^{-1} and the G band is between 1596 cm^{-1} and 1585 cm^{-1}, the D band for rGO-based systems is between 1329 cm^{-1} and 1332 cm^{-1} and the G band varies minimally and remains approximately at 1596 cm^{-1}, which is within the spectral resolution. On the other hand, the 2D band changes rather strongly between the manganese oxides on GO (2694 cm^{-1} to 2664 cm^{-1}) and rGO (2640 cm^{-1} to 2625 cm^{-1}) supports. The frequency-integrated intensity ratios (I_D/I_G and I_G/I_{2D}) of the D and 2D bands show strong dependence for the manganese oxides on GO (0.9 to 1.8 and 9 to 15) and rGO (0.9 to 1.3 and 7 to 9) supports. The I_D/I_G ratio follows an E_L^{-4} relation. This inverse relation of I_D/I_G to the

Table II. Summary of Raman vibrational frequencies of free and graphene-supported manganese oxides

Oxide (Free)	Oxide (Supported)	Raman Shift (cm^{-1})						Ref.
β-MnO_2			392 w	523 m	585 s	633 w	665 m 697 w	This work
			410 m	510 w	576 s	633–640 w		
					580 m			
	GO				580 m	620 m	665 w	This work
	rGO		392 m			620 w	665 m	This work
Mn_3O_4		319 w	374 w			650 m	659 s	63
							650 s	64
		316 w	368 w					
		310–315 w	365 w				651 s	63
		314 m	376 m				654 s	This work
	GO				580 m		654 m	This work
	rGO		376 m		473 m		654 s	This work
α-Mn_2O_3		311 w		509 m	565 w	653 w	672 s 697 w	63
					581 s	650 w	680 m	64
						650 s		63
γ-Mn_2O_3						633 s	650 m	63
MnO				544 m	595 w		645 w	63
				537 s				
				521 s				

Letter s, m, and w stand for strong, medium, and weak band intensity, respectively.

fourth power of the laser energy was previously reported in a Raman study of nanographite.[79,80] Based on Raman scattering theory calculations, the matrix elements associated with the double-resonance Raman processes of the D band show an E_L dependence of E_L^{-4} for nanographite.[79] The 2D band is predicted to have an excitation energy dependence of E_L^{-3}.[81] Here we refer to this as the 2D band to signify that it is the second-order or first overtone of the D band. Although the I_{Mn}/I_G ratio was 0.2 for most samples, Mn_3O_4/GO exhibited a large value of 1.8 due to the thicker Mn area. We also made an attempt to determine the nature of the defects by plotting the 2D band position with the G band (Fig. 9g). It is safe to say that the defects are of residual or *p*-type for the GO-based hybrids, while the rGO-based hybrids exhibited *n*-type defects (i.e., the G band increased and the 2D band decreased).[82] The sensitivity of the Raman analysis of these samples is one of the reasons for the difference between the Raman and XRD phase identifications. The XRD diffractograms revealed the presence of only bulk phases, whereas the Raman spectra allow the identification of other surface manganese oxide species. The Raman mapping of two of the hybrid samples is shown as a representative example indicative of the surface or spatial uniformity/inhomogeneity, thus indirectly measuring the elemental composition similar to EDS (Fig. 10). The sharpness and almost uniform intensity maps of the D, G, and Mn bands (corrected for baseline while generating the maps) contoured at the boundary of GO domains and layers are indicative of a higher degree of crystallinity/order and thus the intrinsic nature of the GO layers and manganese oxide nanoparticles supported upon them. Our results regarding the Raman frequencies of the manganese oxides together with previous literature data are presented in Table II. It is also worth noting that the map of the intensity ratio of the Mn versus G peak (referred to as sp^2-bonded carbon) provides an avenue to analyze local charge transfer features that are primarily a consequence of the strong electronic–structural coupling of MnO_2 and Mn_3O_4 and GO functional groups and its influence on the electrochemical activity as discussed below in terms of the electrocatalytic activity of Co_3O_4.[83,84]

Mn_3O_4 has the normal-spinel structure $Mn^{2+}Mn^{3+}O_4$, in which the Mn^{2+} ion in the formula unit occupies the tetrahedral site, while the two Mn^{3+} ions occupy the octahedral sites. Experimental and theoretical measurements have demonstrated that the three low-Miller-index planes ({100}, {110}, and {111}) of such metallic oxide particles with face-centered cubic (fcc) structure differ not only in the surface atomic density but also in the electronic structure, geometric bonding, and chemical and electrochemical reactivity.[85] As a result, those planes have different surface energies, following the order $\gamma\{111\} < \gamma\{100\} < \gamma\{110\}$, which closely parallels the catalytic activities for CO and CH_4 oxidation.[86–89] In catalysis of CO oxidation, the CO molecule interacts preferably with the surface Mn^{3+} cations, which is the only favorable site for CO adsorption, as confirmed theoretically[90,91] and shown experimentally for Co_3O_4.[92] Oxidation of adsorbed CO then occurs by abstraction of the surface oxygen that was coordinated with these Mn^{3+} cations. The partially reduced manganese site, i.e., Mn^{2+} cation with a neighboring oxygen vacancy, is reoxidized by a gas-phase oxygen molecule or oxygen from water molecules in the aqueous electrolyte back to the active, Mn^{3+} form. Consequently, the surface Mn^{3+} cations are regarded as the active sites for CO oxidation, whereas the surface Mn^{2+} cations are almost inactive. It is known that, in the Mn_3O_4 crystal structure, the {001} and {111} planes contain only Mn^{2+} cations, while the {110} plane is composed mainly of Mn^{3+} cations. This scenario has been proved by surface differential diffraction studies concluding that the Mn^{3+} cations are present solely on the {110} plane. Similarly, in our own experiment with the Mn_3O_4/rGO composite electrode, while the electrochemical activity of the Mn_3O_4/rGO (and GO) composites for CO oxidation is by no means optimized, we are tempted to say based on our findings

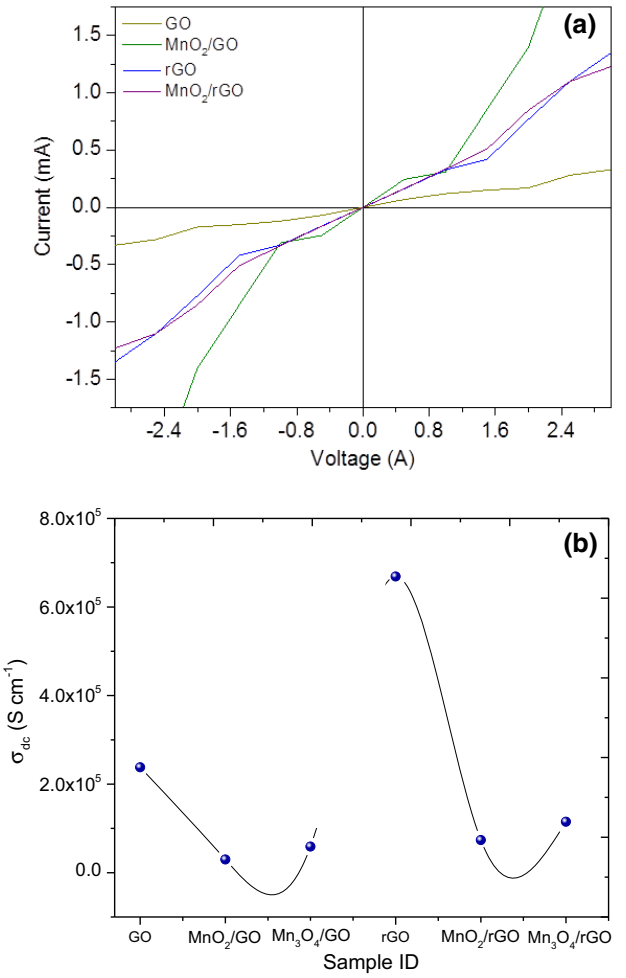

Fig. 11. (Color online). Room-temperature electrical property measurements: (a) *I–V* (current–voltage) and (b) electrical conductivity (σ_{dc}), for all of the samples studied.

that Mn_3O_4 with predominantly {110} exposed surfaces may have higher electrochemical activity for CO oxidation than the sole six {100} exposed surfaces. In sharp contrast, the Mn_3O_4 enclosed by the eight {111} facets on the rGO and GO sheets is expected to exhibit the highest electrochemical activity among the four Mn_3O_4/graphene hybrid electrodes. Theoretically, it is predicted that the electron contributions of Mn_{3d} states prevail, the others being contributions from O_{2p} oxygen states. The contributions of occupied C_{2p} states at the Fermi level turn out to be smaller by two orders of magnitude than the oxygen contributions, having a small value of 0.008, i.e., small, but nonzero. The latter is consistent with the fact that the conductivity of graphene is never smaller than the minimum value of the quantum conductivity unit. Thus, it is possible to suppose that graphene islands can retain their unique properties in the MnO_x (001)/graphene system, which also forms the basis for carbon-containing electronic and magnetic electronic devices.[93] The other implications of this study are relevant to nanoelectronic and spintronic devices, i.e., heterointerfaces of graphene/(ferromagnetic metal or oxide), instead of a nanomagnetic semiconductor or traditional metal. This is ideal for spintronics due to the small spin–orbit interaction as well as the vanishing nuclear magnetic moment of the carbon atom.

Analogous to spectroscopic studies, electrical measurements could provide complementary information on metal oxide–graphitic interfaces besides the dc electrical conductivity (σ_{dc}) of the hybrids. Figure 11 provides the room-temperature I–V measurements for a two-terminal device determining the resistance R_{2t} and the corresponding σ_{dc}. A few interesting and noteworthy features from Fig. 11 are (a) the I–V curves show quasi-semiconducting behavior, in contrast to the ohmic or linear behavior for all of the films, (b) the σ_{dc} of rGO was higher by almost one order of magnitude (7×10^5 S cm) compared with GO (0.1×10^5 S cm), and finally (c) the σ_{dc} of both the rGO- and GO-supported hybrids decreased by a similar magnitude with their presence as anticipated.

CONCLUSIONS

We report the development of hybrid nanomaterials prepared by utilizing graphene derivatives coupled with nano/micro-manganese oxide polymorphs, i.e., β-MnO_2 [Mn(IV)] and Mn_3O_4 [Mn(II, III)], laying the groundwork for high-performance electrochemical electrodes owing to their higher specific capacitance, wide operational potential window and stability through charge–discharge cycling, environmentally benignity, easy processing, and reproducibility on a larger scale. We strategically designed them by direct anchoring on GO and rGO, and this facile approach afforded strong chemical/physical attachment and is expected to provide coupling between the pseudocapacitive transition-metal oxides and supercapacitive nanocarbons and reasonable areal density of tailored interfaces. Using a range of complementary analytical tools, we determined the surface morphology, local (lattice dynamical) and average structure, and local charge transfer owing to the physically (or chemically) adsorbed manganese oxides, highlighting the surface structure, local charge transfer, and properties of interfaces.

ACKNOWLEDGEMENTS

S.G. acknowledges partial financial support from the WKU Research Foundation for start-up funds and an NSF EPSCoR Track RII Award. We thank P. Norris (Advanced Materials Institute, WKU) for AFM training, E. Heintzman for SEM, and Dr. J. Andersland for BEI/EDS measurements.

REFERENCES

1. A.K. Geim and K.S. Novoselov, *Nat. Mater.* 6, 183 (2007).
2. S. Gupta, E. Heintzman, and J. Jasinski, *J. Electron. Mater.* July 4 Issue (2014) and references therein.
3. Y. Zhang, Y.-W. Tan, H.L. Stormer, and P. Kim, *Nature* 438, 201 (2005).
4. M.D. Stoller, S. Park, Y. Zhu, J. An, and R.S. Ruoff, *Nano Lett.* 8, 3498 (2008).
5. C. Lee, X.D. Wei, J.W. Kysar, and J. Hone, *Science* 321, 385 (2008).
6. C. Liu, Z. Yu, D. Neff, A. Zhamu, and B.Z. Jang, *Nano Lett.* 10, 4863 (2010).
7. F. Liu, C. W. Lee, S. S. Im, *J. Nanomater.* 1 (2013).
8. Y. Hou, M. Shao, B.R. Ellis, and B. Yi, *PCCP* 13, 15384 (2011).
9. K.P. Loh, Q.L. Bao, P.K. Ang, and J.X. Yang, *J. Mater. Chem.* 20, 2277 (2010).
10. A. Bagri, C. Mattevi, M. Acik, Y.J. Chabal, M. Chowalla, and V.B. Shenoy, *Nat. Chem.* 2, 581 (2010).
11. K.P. Loh, Q. Bao, G. Eda, and M. Chowalla, *Nat. Chem.* 2, 1015 (2014).
12. G. Eda and M. Chowalla, *Adv. Mater.* 22, 2392 (2010).
13. F. Schwierz, *Nat. Nanotechnol.* 5, 487 (2010).
14. P. Blake, P.D. Brimicombe, R.R. Nair, T.J. Booth, D. Jiang, F. Schedin, L.A. Ponomarenko, S.V. Morozov, H.F. Gleeson, E.W. Hill, A.K. Geim, and K.S. Novoselov, *Nano Lett.* 8, 1704 (2008).
15. A.J. Du, Z.H. Zhu, and S.C. Smith, *J. Am. Chem. Soc.* 132, 2876 (2010).
16. I.V. Pavlidis, T. Vorhaben, D. Gournis, G.K. Papadopoulos, U.T. Bornscheuer, and H. Stamatis, *J. Nanoparticle Res.* 14, 842 (2012).
17. L. Zhang, J. Xia, Q. Zhao, L. Liu, and Z. Zhang, *Small* 6, 537 (2010).
18. Q. Zhang, E. Uchaker, S.L. Candelaria, and C. Guozhong, *Chem. Soc. Rev.* 42, 3127 (2013).
19. B.E. Conway, *Electrochemical Supercapacitors: Scientific Fundamentals and Technological Applications* (New York: Kluwer Academic/Plenum, 1999).
20. L. Nyholm, G. Nyström, A. Mihranya, and M. Strømme, *Adv. Mater.* 23, 3751 (2011).
21. J.T.W. Wang, J.M. Ball, E.M. Barea, A. Abate, J.A.A. Webber, J. Huang, M. Saliba, I.M. Sero, J. Bisquert, H.J. Snaith, and R.J. Nicholas, *Nano Lett.* 14, 724 (2014).
22. M. Liu, R. Zhang, and W. Chen, *Chem. Rev.* 114, 5117 (2014).
23. B. Luo, S.M. Liu, and L.J. Zhi, *Small* 8, 630 (2012).
24. D.A. Dikin, S. Stankovich, E.J. Zimney, R.D. Piner, G.H.B. Dommett, G. Evmenenko, S.T. Nguyen, and R.S. Ruoff, *Nature* 448, 457 (2007).
25. J.T. Robinson, M. Zalalutdinov, J.W. Baldwin, F.K. Perkins, E.S. Snow, Z. Wei, P.E. Sheeshan, and B.H. Houston, *Nano Lett.* 8, 3441 (2008).

26. J.T. Robinson, F.K. Perkins, E.S. Snow, Z. Wei, and P.E. Sheeshan, *Nano Lett.* 8, 3137 (2008).
27. X. Zuo, S. He, D. Li, C. Peng, Q. Huang, S. Song, and C. Fan, *Langmuir* 26, 1936 (2010).
28. C. Jafta, F. Nkosi, L. Roux, M. Mathe, M. Kebede, K. Makgopa, Y. Song, D. Tong, M. Oyama, N. Manyala, S. Chen, and K. Ozoemena, *Electrochim. Acta* 110, 228 (2013).
29. A.H.C. Neto, F. Guinea, N.M.R. Peres, K.S. Novoselov, and A.K. Geim, *Rev. Mod. Phys.* 81, 109 (2009).
30. J. Xia, Q. Kuang, S. Yang, F. Xia, S. Wang, and L. Guo, *Sci. Rep.* 3, 2300 (2013).
31. L. Wang, Y. Li, Z. Han, L. Chen, B. Qian, X. Jiang, J. Pinto, and G. Yang, *J. Mater. Chem. A* 1, 8385 (2013).
32. J.A. Roger and Y.G. Huang, *Proc. Natl. Acad. Sci. USA* 106, 10875 (2009).
33. D.H. Kim, N. Lu, R. Ma, Y.S. Kim, R.H. Kim, S. Wang, J. Wu, S.M. Won, H. Tao, and A. Islam, et al., *Science* 333, 838 (2011).
34. R. Kötz and M. Carlen, *Electrochim. Acta* 45, 2483 (2000).
35. L.-Q. Mai, F. Yang, Y.-L. Zhao, X. Xu, L. Xu, and Y.-Z. Luo, *Nat. Commun.* 2, 381 (2011).
36. V.V.N. Obreja, *Physica E* 40E, 2596 (2008).
37. E. Frackowiak and F. Béguin, *Carbon* 39, 937 (2001).
38. C. Peng, S. Zhang, D. Jewell, and G.Z. Chen, *Prog. Nat. Sci.* 18, 177 (2008).
39. W. Sugimoto, K. Yokoshima, Y. Murakami, and Y. Takasu, *Electrochim. Acta* 52, 1742 (2006).
40. P. Simon and Y. Gogotsi, *Nat. Mater.* 7, 845 (2008).
41. Z.S. Wu, W. Ren, D.W. Wang, F. Li, B. Liu, and H.M. Cheng, *ACS Nano* 4, 5835 (2010).
42. C. Zhu, S. Guo, Y. Fang, L. Han, E. Wang, and S. Dong, *Nano Res.* 4, 648 (2011).
43. X. Lang, A. Hirata, T. Fujita, and M. Chen, *Nat. Nanotechnol.* 6, 232 (2011).
44. Y. Sun, X. Hu, W. Luo, and Y. Huang, *ACS Nano* 5, 7100 (2011).
45. Y. Liang, Y. Li, H. Wang, and H. Dai, *J. Am. Chem. Soc.* 135, 2013 (2013).
46. J. Zhang, J. Jiang, and X.S. Zhao, *J. Phys. Chem. C* 115, 6448 (2011).
47. G. Aminoff, *Z. Kristallgr.* 64, 475 (1927).
48. J. Attenburrow, A.F.B. Cameron, J.H. Chapman, R.M. Evans, B.A. Hems, A.B.A. Jansen, and T. Walker, *J. Chem. Soc.* 1094 (1952).
49. J. Coraux, L. Marty, N. Bendiab, and V. Bouchiat, *Acc. Chem. Res.* 46, 2193 (2013).
50. S. Cui, S. Mao, G. Lu, and J. Chen, *J. Phys. Chem. Lett.* 4, 2441 (2013).
51. V. Sridharm, H.-J. Kim, J.-W. Jung, C. Lee, S. Park, and I.-K. Oh, *ACS Nano* 6, 10562 (2012).
52. Z. Xu, Z. Li, C.M.B. Holt, X. Tan, H. Wang, B.S. Amirkhiz, T. Stephenson, and D. Mitlin, *J. Phys. Chem. Lett.* 3, 2928 (2012).
53. T. Kyotani, K. Suzuki, H. Yamashita, and A. Tomita, *Tanso* 160, 255 (1993).
54. T. Nakajima, A. Mabuchi, and R. Hagiwara, *Carbon* 26, 357 (1988).
55. W. Scholz and H.P.Z. Boehm, *Anorg. Allg. Chem.* 369, 327 (1969).
56. M. Ding, Y. Tang, and A. Star, *J. Phys. Chem. Lett.* 4, 147 (2013).
57. W. Wei, X. Cui, W. Chen, and D.G. Ivey, *Chem. Soc. Rev.* 40, 1697 (2011).
58. W. Hummers and R.J. Offeman, *Am. Chem. Soc.* 80, 1339 (1958).
59. S. Park, J. An, R.J. Potts, A. Velamakanni, S. Murali, and R.S. Ruoff, *Carbon* 49, 3019 (2011).
60. K.E. Carr, *Carbon* 8, 245 (1970).
61. D.C. Marcano, D.V. Kosynkin, J.M. Berlin, A. Sintskii, Z. Sun, A. Slesarev, L.B. Alemany, W. Lu, and J.M. Tour, *ACS Nano* 4, 4806 (2010).
62. M. Ding, Y. Tang, and A. Star, *J. Phys. Chem. Lett.* 4, 147 (2013).
63. H. Lipson and A.R. Stokes, *Nature* 149, 328 (1942).
64. O. Zhou, R.M. Fleming, D.W. Murphy, C.H. Chen, R.C. Haddon, and A.P. Ramirez, *Science* 263, 1744 (1994).
65. F. Buciuman, F. Patcas, R. Cracium, and D.R.T. Zahn, *Phys. Chem. Chem. Phys.* 1, 185 (1999).
66. C. Julien, M. Massot, R. Baddour-Hadjean, S. Franger, S. Bach, and J.P. Pereira-Ramos, *Solid State Ion.* 159, 345 (2003).
67. C. Julien, M. Massot, S. Rangan, M. Lemal, and D. Guyomard, *J. Raman Spectrosc.* 33, 223 (2002).
68. C.M. Julien, M. Massot, and C. Poinsignon, *Spectrochim. Acta. A* 60, 689 (2004).
69. A.C. Ferrari, *Solid State Commun.* 143, 47 (2007).
70. Z.W. Chen, J.K.L. Lai, and C.H. Shek, *Appl. Phys. Lett.* 86, 181911 (2005).
71. B.R. Strohmeier and D.M. Hercules, *J. Phys. Chem.* 88, 4923 (1988).
72. F. Kapteijn, A.D. Van Langeveld, J.A. Moulijn, A. Andreini, M.A. Vuurman, A.M. Turek, J.-M. Jehng, and I.E. Wachs, *J. Catal.* 150, 94 (1994).
73. D. Gosztola and M.J. Weaver, *J. Electroanal. Chem. Interfacial Electrochem.* 271, 141 (1989).
74. M.-C. Bernard, A.H.L. Go, V.B. Thi, and S.C. de Torresi, *J. Electrochem. Soc.* 140, 3065 (1993).
75. W.B. White and V.G. Keramidas, *Spectrochim. Acta A* 28, 501 (1972).
76. I. Rusakova, T.O. Ely, C. Hofmann, D.P. Centurion, C.S. Levin, N.J. Halas, A. Luttge, and K.H. Whitmire, *Chem. Mater.* 19, 1369 (2007).
77. C.M. Julien and M. Massot, *J. Phys. Condens. Matter* 15, 3151 (2003).
78. D.P. Dubal, D.S. Dhawale, R.R. Salunkhe, and C.D. Lokhande, *J. Alloys Compd.* 496, 370 (2010).
79. L.G. Cancado, K. Takai, T. Enoki, M. Endo, Y.A. Kim, H. Mizusaki, A. Jorio, L.N. Coelho, R. Magalhaes-Paniago, and M.A. Pimenta, *Appl. Phys. Lett.* 88, 163106 (2006).
80. K. Sato, R. Saito, Y. Oyama, J. Jiang, L.G. Cancado, M.A. Pimenta, A. Jorio, G. Ge Samsonidze, G. Dresselhaus, and M.S. Dresselhaus, *Chem. Phys. Lett.* 427, 117 (2006).
81. J.S. Park, A. Reina, R. Saito, J. Kong, G. Dresselhaus, and M.S. Dresselhaus, *Carbon* 47, 1303 (2009).
82. M.W. Iqbal, A.K. Singh, M.Z. Iqbal, and J. Eom, *J. Phys. Condens. Matter* 24, 335301 (2012).
83. X.F. Tang, J.H. Li, and J.M. Hao, *Mater. Res. Bull.* 43, 2912 (2008).
84. Y. Sun, P. Lv, J.-Y. Yang, L. He, J.-C. Nie, X. Liu, and Y. Li, *Chem. Commun.* 47, 11279 (2011).
85. X.F. Tang, J.H. Li, and J.M. Hao, *Mater. Res. Bull.* 43, 2912 (2008).
86. X.W. Xie, Y. Li, and Z.Q. Liu, *Nature* 458, 746 (2009).
87. L.H. Hu, Q. Peng, and Y.D. Li, *J. Am. Chem. Soc.* 130, 16136 (2008).
88. L. Hu, K. Sun, Q. Peng, B. Xu, and Y. Li, *Nano Res.* 3, 363 (2010).
89. J. Jansson, *J. Catal.* 194, 55 (2000).
90. P. Broqvist, I. Panas, and H. Persson, *J. Catal.* 210, 198 (2002).
91. M.C. Toroker, D.A. Kanan, N. Alidoust, L.Y. Isseroff, P. Liao, and E.A. Carter, *Phys. Chem. Chem. Phys.* 13, 16644 (2011).
92. F. Grillo, M.M. Natile, and B. Glisenti, *Appl. Catal. B* 48, 267 (2004).
93. V.V. Ilyasov, D.A. Velikokhatskii, I.V. Ershov, I.Y. Nikiforov, and T.P. Zhdanova, *J. Struct. Chem.* 52, 849 (2011); *ibid. J. Mod. Phys.* 2, 1120 (2011).